Nanoscale

PAPER

View Article Online
View Journal | View Issue

Cite this: *Nanoscale*, 2025, **17**, 27225

Controlled colloidal synthesis of anisotropic mixed-metal chalcohalides: insights into morphology and phase evolution

Davide Pratolongo,[a] Ankita Bora,[b] Suvodeep Sen,[b] Niraj Nitish Patil,[b] Stefano Alberti,[a] Manoj Palabathuni,[b] Federico Locardi[a] and Shalini Singh *[b]

Received 11th September 2025,
Accepted 5th November 2025

DOI: 10.1039/d5nr03842a

rsc.li/nanoscale

Mixed-metal chalcohalides have recently emerged as promising semiconductor materials for optoelectronic applications owing to their tunable bandgaps, earth-abundant composition, stability, and relatively low toxicity. Despite these advantages, the synthesis of quaternary chalcohalides remains challenging due to their complex phase chemistry and the thermodynamic preference for binary and ternary secondary by-products, which frequently compete with the preferred quaternary phase formation. In this work, we report the colloidal synthesis of $Sn_2SbS_2I_3$ microcrystals *via* a dual hot-injection method. Our approach yields uniform, crystalline microrods with well-defined morphology and a direct optical band gap of 1.74 eV, placing them within the ideal range for photovoltaic and photodetection applications. By systematically monitoring the reaction mixture during synthesis, we elucidate the growth pathway of $Sn_2SbS_2I_3$. The process initiates with the formation of Sb_2S_3 seeds, which subsequently undergo compositional transformation through incorporation of Sn^{2+} and I^- in their structure. This progressive substitution and intercalation drive the conversion toward the quaternary $Sn_2SbS_2I_3$ phase, highlighting a seed-mediated growth mechanism.

Introduction

Chalcohalide materials represent a unique class of semiconductors distinguished by the simultaneous incorporation of chalcogen elements (S, Se, Te) and halogens (Cl, Br, I) within their crystal structure. This dual-element composition imparts these materials with intriguing structural diversity and tunable electronic properties, positioning them as promising candidates for next-generation optoelectronic and energy applications. Based on their elemental composition, chalcohalide materials can be systematically classified into several subgroups: heavy Pnictogen chalcohalide, transition and post-transition metal chalcohalide, mixed-metal chalcohalide, and hybrid organic–inorganic metal chalcohalide.[1,2] Although metal chalcohalides have long been known,[3,4] unlike their chalcogenide counterparts, the controlled synthesis and the underlying nucleation and growth mechanisms of chalcohalides remain poorly explored.[5–7] It is only within the past decade that they have gained significant attention as promising candidates to replace lead halide perovskites (LHPs).[1,8–11]

LHPs, generally represented as $APbX_3$ (A = Cs, Rb, methylammonium or formamidinium and X = Cl, Br or I),[8,12–16] are widely studied as semiconductors in a range of optoelectronic applications, including light-emitting diodes (LEDs),[17,18] solar cells,[12,17–21] lasers,[22–24] and photodetectors.[25,26] They possess excellent optoelectronic properties, among which the tunability of their absorption and emission spectra from the visible to near infrared region is particularly important.[17,27,28] Additionally, the ability to control the size of LHPs down to the quantum confinement regime makes this class of materials even more fascinating, as their optoelectronic properties can be further tailored.[8,17,29,30] Nevertheless, the urgency to replace LHPs stems from two primary limitations: the intrinsic toxicity of lead, which poses serious environmental and health risks, and the poor stability of LHPs under ambient conditions.[31,32] In contrast, chalcohalide materials offer a promising solution by addressing both challenges while maintaining comparable optoelectronic properties. Similar to LHPs, chalcohalides exhibit high charge carrier mobility and defect tolerance properties largely attributed to the highly dispersed nature of the valence band (VB) and conduction band (CB) states.[1–4,8–11] The enhanced stability, however, is largely due to the presence of the chalcogen (Ch) anion, which interacts with the metal–halide bonds within the material. Specifically, the chalcogen forms a bond with the metal after it

[a]*Dipartimento di Chimica e Chimica Industriale, Università degli Studi di Genova, Via Dodecaneso 31, I-16146 Genova, Italy*
[b]*Bernal Institute & School of Chemical Sciences, University of Limerick, Sreelane, V94 T9PX Limerick, Ireland. E-mail: shalini.singh@ul.ie*

donates an electron to the halide, thereby enhancing the overall structural robustness of the compound.[1,33,34] Moreover, in the Sn-based chalcohalide, the chalcogen ion plays a critical role in preventing the oxidation of Sn^{2+} to Sn^{4+}, which is a key factor contributing to the long-term stability of the material.[35] The mixed-metal chalcohalide offers enhanced tunability of the material properties through compositional variation not only of the anionic species, but also of the metal counterparts.[1,35,36] Recent work by Nie *et al.* has demonstrated the potential of the mixed-metal chalcohalide $Sn_2SbS_2I_3$ in photovoltaics, achieving a power conversion efficiency (PCE) of ~4%,[37] a value comparable to the first LHP solar cell.[12]

$Sn_2SbS_2I_3$ can crystallize as two polymorphs, namely *Cmcm* (orthorhombic) or $Cmc2_1$ (monoclinic), each exhibiting unique structural properties. In the *Cmcm* structure, $(Sn_2S_2I_2)_n$ forms chains along the *a*-axis, which are tightly interconnected by Sb and I, as Fig. S1 shows. The final structure growth on the *ab*-plane, thereby resulting in the final stoichiometry composition. Conversely, in the $Cmc2_1$ polymorph, the environmental coordination sphere of Sb and Sn differs significantly from those in the *Cmcm* structure, which leads to the formation of $(Sn_2SbS_2I_3)_n$ chains aligned along the *a*-axis.[1,3,12,36,38,39] Density Functional Theory (DFT) calculations predict a band gap of 1.80 eV and 1.08 eV for the *Cmcm* and $Cmc2_1$ structure, respectively.[36,38]

However, experimental measurements of orthorhombic $Sn_2SbS_2I_3$ reveal a slightly different band gap of 1.45 eV.[34] A notable feature of these polymorphs is their direct band gap, which contrasts with the typically indirect band gaps found in many chalcohalide compounds, particularly those lacking a mixed-metal composition.[38,40–44] $Sn_2SbS_2I_3$ was first synthesized in 1980 by Oliver-Fourcade *et al. via* solid-state reaction as a *Cmcm* orthorhombic crystal structure.[3] More recent efforts have expanded its synthesis to alternative methods, including thin film fabrication from solution-[37] and chemical vapor transport.[36] However, the preparation of the mixed metals chalcohalide, such as $Sn_2SbS_2I_3$, remains challenging due to the need for precise control over the reaction parameters to allow the balance between the reactivity of metal and anionic precursors in solution. This difficulty often results in phase impurities, such as the formation of secondary binary or ternary by-products, which can significantly hinder the material's performance in optoelectronic devices.[45]

In this study, we report the colloidal synthesis of $Sn_2SbS_2I_3$ microrods *via* a dual hot-injection method. In this approach, antimony (Sb) and sulfur (S) precursors are co-injected into a pre-heated solution of SnI_2 and organic ligands at 240 °C. The employment of a colloidal synthesis approach, specifically, the hot-injection method, enables fine-tuning of reaction conditions to precisely control the size, morphology, and phase purity of the resulting product.[45–55] To elucidate the formation mechanism of $Sn_2SbS_2I_3$, the reaction mixture was monitored at various stages post-injection using X-ray diffraction (XRD) and scanning electron microscopy (SEM). These techniques provided detailed insights into the crystalline phase evolution and morphological development, revealing key intermediate phases and structural transformation pathways. These findings demonstrate the viability of a controlled colloidal route for accessing complex chalcohalide semiconductors. Furthermore, the detailed mechanistic insights into their crystallization pathway could inform the rational design of related materials for optoelectronic devices.

Results and discussion

$Sn_2SbS_2I_3$ microrods were synthesized using a hot injection approach in which antimony(III) acetate ($Sb(OA)_3$) and oleylamine sulphur (OLA-S) solutions were injected at 240 °C into a reaction mixture of SnI_2, oleyl amine (OLA) and oleic acid (OA) as ligands, and 1-octadecene (ODE) as solvent (see Experimental section for details). The synthesis involves the consecutive injection of $Sb(OA)_3$ followed by OLA-S after 5 s (Fig. 1a), a strategy designed to suppress premature redox reactions between the antimony and sulfur precursors and Sn^{2+} ions prior to the onset of the reaction. This controlled injection sequence is critical for maintaining the desired oxidation states and ensuring phase-pure product formation.

The as-synthesised $Sn_2SbS_2I_3$ microrods were analysed by XRD (Fig. 1b). The experimental pattern of the synthesised

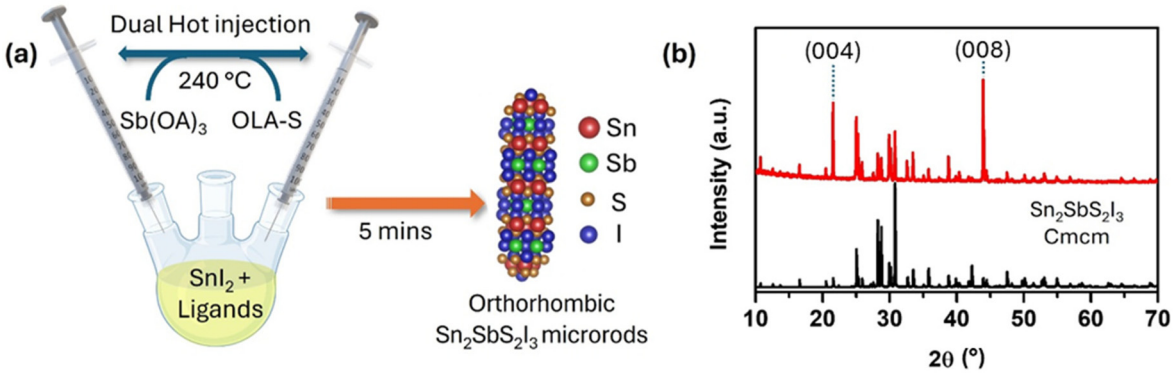

Fig. 1 (a) Scheme of the colloidal dual hot-injection protocol for $Sn_2SbS_2I_3$ microrods synthesis; (b) XRD spectra of the as-synthesised $Sn_2SbS_2I_3$ microrods (red) and the $Sn_2SbS_2I_3$ *Cmcm* reference (ICSD number 23344).

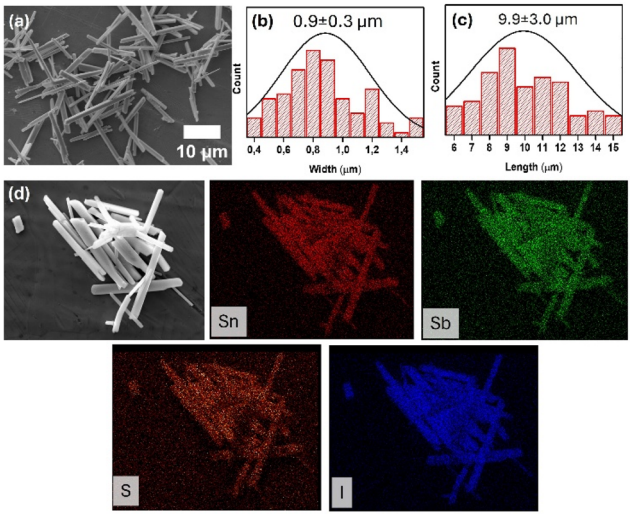

Fig. 2 (a) SEM micrograph of the as-synthesised $Sn_2SbS_2I_3$ rods, (b and c) size histograms of the width and length of the microrods, respectively, (d) elemental mapping by SEM-EDX of Sn (red), Sb (green), S (orange), and I (blue) along the $Sn_2SbS_2I_3$ rods.

$Sn_2SbS_2I_3$ displayed characteristic peaks of the *Cmcm* orthorhombic phase (ICSD number 23344). The intensity differences with respect to the reference pattern can be ascribed to a preferential orientation of the microrods on the sample holder. $Sn_2SbS_2I_3$ crystallizes in the *Cmcm* phase, in which $Sn_2S_2I_2$ chains run along the *a*-axis. Since the microrods tend to lie flat on the sample holder, a preferential orientation is expected. Experimentally, the two most intense peaks in the reference pattern at 28.2° and 30.8°, corresponding to the (130) and (114) reflections (Fig. S2 and S3), appear significantly reduced in the measured sample. In contrast, reflections with a strong *c*-axis component, such as those at 21.6°, and especially 44.0°, assigned to the (004), and (008) planes, respectively, exhibit markedly increased intensity. A milder enhancement is also observed for the peaks at 10.7° and 32.6°, indexed as (002) and (006), respectively. On the (004) plane, Sb and I atoms are located, which interconnect the $Sn_2S_2I_2$ chains (Fig. S1). This behaviour suggests a preferential growth or elongation of the particles along the planes perpendicular to the *c*-axis, indicative of the formation of anisotropic structures. Selected area electron diffraction (SAED) pattern (Fig. S4) of the microrods along the [1$\bar{1}$0] axis shows (008) reflections along with high order reflection planes. Moreover, no peaks were observed in the XRD experimental pattern related to impurities such as secondary binary or ternary by-products (Sb_2S_3, SbSI, Sn_2SI_2, Sn_4SI_6, SnS, SnI_2 *etc.*), as shown in Fig. S4. Also, the absence of peaks related to the monoclinic $Cmc2_1$ phase of $Sn_2SbS_2I_3$ confirms the phase and composition purity of the synthesised materials.

Fig. 2a represents the SEM image of the as-synthesised $Sn_2SbS_2I_3$ microrods revealing a rod-like morphology of the synthesized $Sn_2SbS_2I_3$. The rods have an average length of 9.9 ± 3.0 μm and a width of 0.9 ± 0.3 μm (Fig. 2b and c). SEM-EDX analysis shows a uniform elemental distribution along the rods (Fig. 2d). The ratio of the calculated atomic percentages corresponds to a final material stoichiometry of $Sn_{1.65}SbS_{2.16}I_{2.56}$. Therefore, the as-synthesized material appears to be slightly enriched in Sb and S (Table S1).

Furthermore, X-ray photoelectron spectroscopy (XPS) analysis was obtained to gain insight into the elemental composition, chemical structure, and electronic state of the different elements in the as-synthesised microrods (Fig. 3 and S5). Surface analysis reveals a composition of $Sn_{1.56}SbS_{1.78}I_{2.24}$. This result indicates that the surface of the rods is even richer in Sb than the bulk of the microcrystals. Conversely, the S content is lower at the surface. The high-resolution XPS spectra in the Sb 3d region (Fig. 3a) display peaks centred at 540 eV and 541.5 eV. This corresponds to the same Sb(v) species with the apparent splitting attributed to differential splitting. The high-resolution XPS analysis of the Sn 3d region (Fig. 3b) illustrates the peaks associated with the spin–orbit doublet levels Sn $3d_{5/2}$ and Sn $3d_{3/2}$, located at 487.5 eV and 496.0 eV, respectively, with an energy separation of approximately 8.5 eV.[56] The S 2p region (Fig. 3c) exhibits a peak at 163.2 eV, which arises from the typical S 2p doublet, with the $2p_{3/2}$ and $2p_{1/2}$ components located at 163.1 eV and 165.4 eV, respectively, and separated by 2.3 eV, in line with the presence of S^{2-}. Finally, the I 3d region (Fig. 3d) shows a well-defined doublet derived from the spin–orbit split levels I $3d_{5/2}$ and I $3d_{3/2}$ at 620.1 eV and 631.4 eV, respectively, with an energy separation of 11.3 eV, consistent with the presence of I^-. The

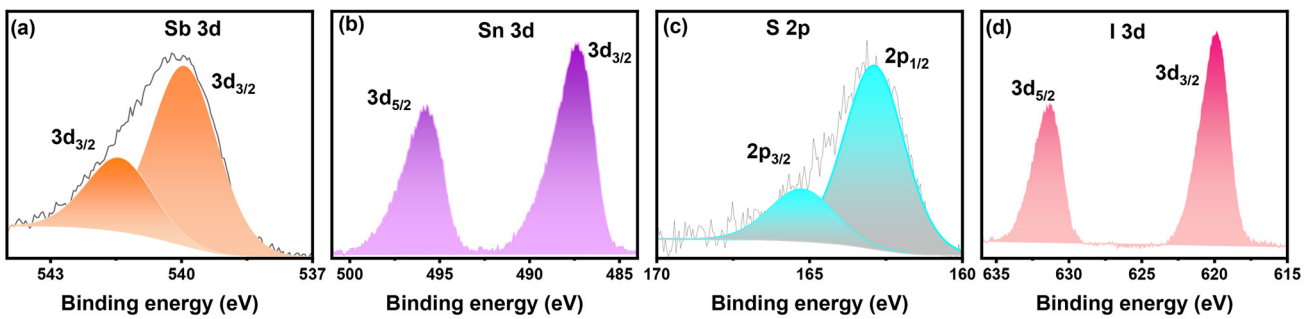

Fig. 3 High-resolution XPS spectra of $Sn_2SbS_2I_3$ rods (a) Sb 3d, (b) Sn 3d, (c) S 2p, and (d) I 3d.

absence of additional features related to surface oxidation, binary/ternary metal oxides, or other by-products in high-resolution XPS analysis reflects very positively on the robustness of the dual injection approach developed in this research for the synthesis of metal chalcohalides.

The reflectance spectrum of $Sn_2SbS_2I_3$ rods is reported in Fig. 4a and is characterized by a drop in reflectance between 600–800 nm, consistent with the onset of electronic transition from the valence band to the conduction band. No additional peaks are observed, confirming the phase purity of the synthesized material. The Tauc plot shown in Fig. 4b, derived from the manipulation of the reflectance spectrum by the Kubelka–Munk transformation and assuming a direct allowed transition, reveals an optical band gap of 1.74 eV. This value is in good agreement with the 1.80 eV band gap calculated for *Cmcm* orthorhombic $Sn_2SbS_2I_3$.[36] The slight discrepancy in the band gap may be attributed to several factors. The anisotropic morphology of the synthesized $Sn_2SbS_2I_3$ could influence its electronic states, even though the particle size is far from the quantum confinement regime. The effect of rod-like morphology was demonstrated by Tsai *et al.* on TiO_2 nanorods, which exhibit diameters larger than the Bohr radius of that semiconductor.[57] In particular, their reflectance analysis revealed spectra with features that vary depending on the nanorod length and differ from those of the bulk semiconductor. Moreover, Nicolson *et al.* reported that static cationic disorder in this class of materials, when synthesized at temperatures above 127 °C, leads to a reduction in the band gap.[36] Furthermore, as demonstrated by SEM-EDX and XPS analyses, the atomic composition at the surface and throughout the crystal does not perfectly match the nominal $Sn_2SbS_2I_3$ stoichiometry. According to the density of states (DOS) analysis reported by Kavanagh *et al.*, the conduction band minimum (CBM) of $Sn_2SbS_2I_3$ is mainly formed by interactions among Sb p and I p orbitals, whereas the valence band maximum (VBM) is predominantly influenced by the antibonding interactions between the Sn $5s^2$ lone pair, S^{2-} and I^- p states.[1,36,38] Consequently, all these ions participate in the formation of the frontier bands; thus, variations in their relative proportions may modify the electronic state energies, leading to a different band gap. Given this, we assume that the bandgap discrepancy observed here is due to a combination of morphology-induced electronic effect and thermally driven cation disorder.

FTIR spectrum of as-synthetised $Sn_2SbS_2I_3$, shown in Fig. S6, was acquired in the range 500–4000 cm^{-1} to investigate the organic fraction bound to the microrods surface. In particular, the peaks at 2955, 2920, 2850 cm^{-1} are attributed to C–H stretching vibration, while the band at 1450 cm^{-1} corresponds to the C–H bending of the aliphatic chains of the ligands. Additional information on the nature of the bound ligands can be obtained from the 1700–1300 cm^{-1} region. The peak at 1630 cm^{-1} is associated with the asymmetric bending of N–H group, indicating the presence of amine functionalities. Notably, the absence of a peak around 1700 cm^{-1}, characteristic of C=O bending in oleic acid, suggests a low concentration or absence of this ligand on the microrod surface. Finally, the broad peak observed at 1040 cm^{-1}, located in the fingerprint area, does not allow for a clear distinction between OLA and OA due to its broad and non-specific nature.

To follow the progress of the reaction and to investigate the kinetic factors governing the formation pathway for the $Sn_2SbS_2I_3$ microrod formation, aliquot studies were conducted. Each aliquot was purified (as described in the Experimental section) and was subsequently analysed by XRD and SEM (Fig. 5), providing insights into both the crystal phase and morphology evolution over the course of the reaction. Upon the simultaneous injection of $Sb(OA)_3$ and OLA-S into the reaction flask containing SnI_2, OLA, and OA at 240 °C, rapid formation of Sb_2S_3 was observed. XRD patterns confirm the presence of the orthorhombic *Pnma* phase of Sb_2S_3 for up to 45 seconds after injection. The corresponding SEM images, as shown in Fig. 5b, c, and Fig. S7 illustrate the formation of microrods with narrow size distribution. No incorporation of Sn in Sb_2S_3 or formation of tin sulphide was observed in the

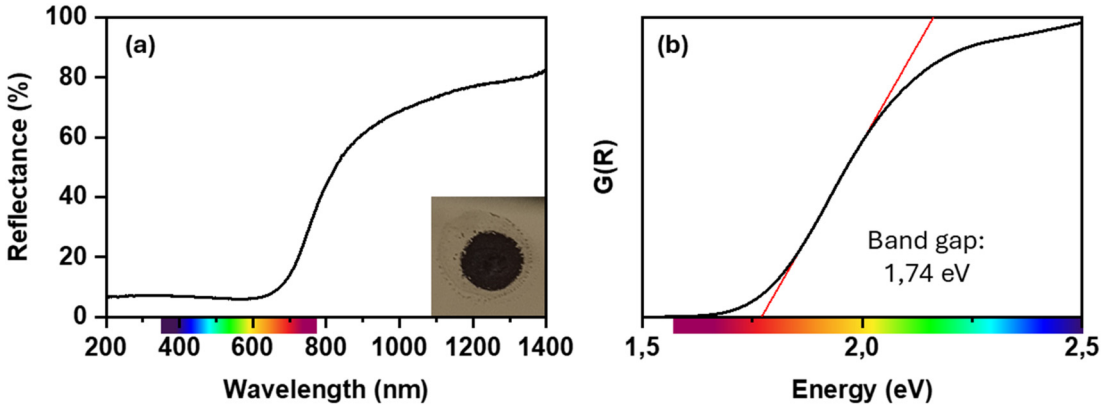

Fig. 4 (a) Reflectance spectra of $Sn_2SbS_2I_3$ microrods, the inset in (a) is a picture of the dry product on zero-background silica wafer, (b) Tauc Plot derived from the reflectance spectra by Kubelka–Munk function ($y = G(R) = (F(R) \times h\nu)^2$ with $F(R) = (1 - (\text{reflectance}/100))^2/(2 \times (\text{reflectance}/100))$ and $x = h\nu = 1240$ (eV × nm)/wavelength). Band gap of 1.74 eV was calculated from the Tauc plot by the extrapolation at $y = 0$ of the graph's linear region (red line).

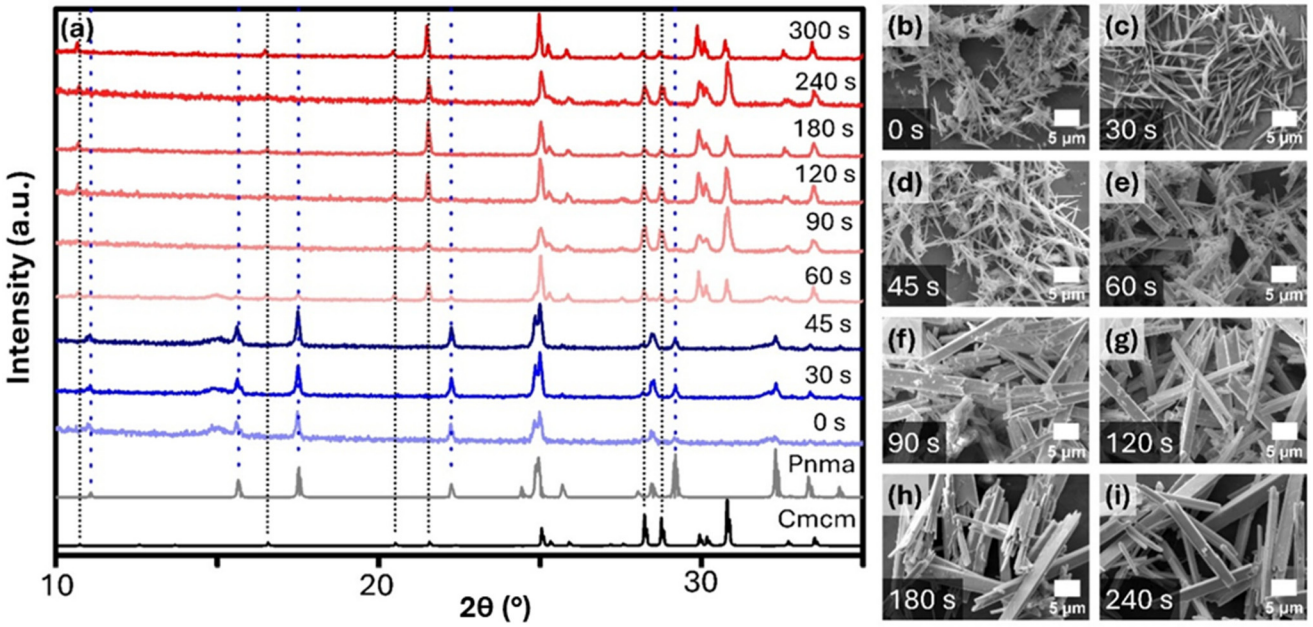

Fig. 5 Analysis of the reaction progression through aliquots taken at different times from the reaction mixture by (a) XRD pattern comparison of $Sn_2SbS_2I_3$ *Cmcm* reference (ICSD number 23344), Sb_2S_3 *Pnma* reference (ICSD number 22176) and the aliquots. The peaks of $Sn_2SbS_2I_3$ *Cmcm* reference and Sb_2S_3 *Pnma* reference are highlighted by a pointed black line and dashed blue line along the graph, respectively. The lines guide to the peaks assignment in the XRD pattern of the aliquots taken to different times; SEM micrography of the aliquots taken at (b) 0 s, (c) 30 s, (d) 45 s, (e) 60 s, (f) 90 s, (g) 120 s, (h) 180 s, (i) 240 s.

first 45 s. However, Sb_2S_3 crystals are short-lived, and between 45 and 90 seconds, XRD patterns indicate the coexistence of both Sb_2S_3 and the final quaternary chalcohalide ($Sn_2SbS_2I_3$). The size distribution of microrods (Fig. 5d and e) shows a wider size distribution, confirming the mixed phase present in the aliquots. After 90 s, the XRD spectra show the gradual disappearance of peaks corresponding to Sb_2S_3 and the emergence of distinct peaks solely corresponding to $Sn_2SbS_2I_3$. The SEM images of the aliquots in Fig. 5f–i showed expansion in the dimensions (length and breadth) and re-tuning of the size distribution. With this experimental evidence, it can be postulated that the reaction begins with the disintegration of SnI_2 in the flask. With a bond dissociation energy between 200–250 kJ mol^{-1}, SnI_2 is most likely to dissociate at 240 °C before the injection of Sb and S precursors in the reaction flask. The Sn^{2+} and I^- ionic species are stabilized by OA and OLA. Once the Sb and S precursors are injected, OLA reduces $Sb(OA)_3$, resulting in the formation of a transient metal–amido complex that gets sulfurized by the injected sulphur precursor, forming anisotropic Sb_2S_3 crystals instantly. However, in the presence of reactive Sn and halogen species and OLA, Sb_2S_3 most likely undergoes partial dissolution, followed by reprecipitation into the final mixed chalcohalide compound consisting of both Sn and Sb. With further time allowed for growing, the ripening process occurs, narrowing down the size distribution.

Parallel to studying the mechanistic pathway, various control experiments with variations in the key parameters were performed to investigate how different reaction parameters interact during synthesis to control the reaction outcome and to identify any correlations between experimental parameters. The details on the variation in reaction parameters are summarized in Table S2. To our surprise, the different set of variations in concentration of ligands (OLA, OA respectively), growth temperature, and time or dilution of the reaction mixture result in the formation of $Sn_2SbS_2I_3$. The only effect of these variations was observed on the morphology of the anisotropic crystals. For instance, reducing the OA concentration to half leads to an increase in length, while doubling the OA concentration resulted in a wider size distribution of the final microrods' length. Acid–base interactions play a crucial role in defining crystal morphology, especially at the nanoscale,[58] since they generate oleate anions and oleyl ammonium cations (OLA-H). FTIR analysis indicates a stronger presence of amine species compared to acid-bonded ones on the microrod surface, suggesting that OLA and OLA-H are the dominant species governing surface coverage and, consequently, the final morphology and size distribution. XPS analysis in Fig. S5 reveals a microcrystal surface with an elemental distribution that reflects the bulky stoichiometry of the final material. Approximately 39% of the surface consists of elements that preferentially act as Lewis acids, such as Sn^{2+} and Sb^{3+}; instead, S^{2-} is a Brønsted acid and should have a better interaction with ammonium species, and I^- does not have a preferential affinity with either amine or ammonium. Furthermore, the activity of S^{2-} as an acid is disfavoured from the coordination in the crystal structure. On the other side, Sn^{2+} and Sb^{3+} can form coordination complexes with electron-pair donors, like amine groups,[59–63] which bind the microrod

surface as L-type ligands.[64] The observed large quantity of amine reflects the possibility of better passivation and stabilization along a longer microrod. However, an excessive concentration of amine beyond the optimal limit for the synthesis of chalcohalides leads to an incomplete conversion of Sb_2S_3 into $Sn_2SbS_2I_3$ (Fig. S8, entry S1, and S9a) since Sn^{2+} and the Sb_2S_3 particles are highly stabilized and do not allow the reaction to complete.

Conclusions

In summary, we have developed a reliable colloidal synthesis strategy for producing phase-pure $Sn_2SbS_2I_3$ microrods using a dual hot-injection method. By carefully tuning the injection conditions and precursor chemistry, we achieved controlled growth of uniform anisotropic structures.

Through systematic investigation of the reaction system by the study of the product evolution, we elucidated the underlying formation mechanism of this complex chalcohalide material. The synthesis process begins with the rapid nucleation of needle-like Sb_2S_3 seeds immediately after the injection of the antimony and sulfur precursors. These initial seeds display a short-lived stability before undergoing partial dissolution. This process triggers a reassembly mechanism in which the incorporation of Sn^{2+} and I^- ions from the reaction mixture drives the transformation of the binary Sb_2S_3 phase into the final quaternary $Sn_2SbS_2I_3$ product and its precipitation as phase-pure crystalline microrods.

This work paves the way for the synthesis of other quaternary chalco-halide, suggesting that the hot injection method is an easy method to control the stoichiometry of the final products.

Experimental section

Materials

Antimony(III) acetate ($Sb(OAc)_3$, Sigma-Aldrich, 99.99%), hexane (Hex, Honeywell, ≥97.0%), isopropanol (iPrOH, Honeywell, ≥99.9%), 1-octadecene (ODE, Sigma-Aldrich, for synthesis), oleic acid (OA, Sigma-Aldrich, 90% technical grade), oleyl amine (OLA, Sigma-Aldrich, 70%), sulphur powder (S powder, TCI, >99.0%), tin(II) iodine (SnI_2, Sigma-Aldrich, 99.99%).

Preparation of sulphur precursor (OLA-S)

A stock solution of sulphur precursor was prepared using 160.1 mg (4.99 mmol) of S powder and 5 mL of OLA. The mixture was loaded in a 10 mL vial and kept under stirring at room temperature in an Ar-filled glove box. The precursor solution changes from a turbid yellow colour to a clear dark red colour after 2 h. The final transparent dark red solution (1 M) was stored in the glove box and used as a stock solution for the $Sn_2SbS_2I_3$ synthesis.

Preparation of antimony oleate ($Sb(OA)_3$)

434.5 mg (1.45 mmol) of $Sb(OAc)_3$ and 5 mL of OA were loaded in a 25 mL 3-neck flask connected to a Schlenk line. The reaction mixture was heated at 100 °C under vacuum and stirring and manteined under these conditions for 1h. The final transparent pale-yellow solution (0.3 M) was transferred into the glove box and used as a stock solution for the $Sn_2SbS_2I_3$ synthesis.

Synthesis of $Sn_2SbS_2I_3$ microrods

75.5 mg (0.20 mmol) of SnI_2, 1.5 mL of OA, 0.5 mL of OLA, and 5 mL of ODE were loaded in a 25 mL 3-neck flask connected to a Schlenk line. The reaction mixture was stirred under vacuum at 120 °C for 30 min. Subsequently, the reaction temperature was raised to 240 °C under an Ar atmosphere, during which the mixture turned its colour from yellow to orange. At this temperature, 0.35 mL of $Sb(OA)_3$ (0.3 M) was swiftly injected into the reaction mixture, and, after 5 s, 0.2 mL of OLA-S (1 M) was swiftly injected, too. After 5 min, the reaction was quenched using an ice bath. The final black coloured reaction mixture was centrifuged at 5000 rpm for 3 min. The obtained precipitate was washed with a solution of Hex : iPrOH (1 : 2) three times. The final black precipitate was dried and stored under environmental conditions for further characterization.

X-ray diffraction (XRD) analysis

The XRD patterns were recorded in an Empyrean X-ray diffractometer. The samples were prepared by drop casting the final product dispersed in hexane on a zero-background boron-doped P-type Silica wafer. The diffractograms were acquired using a 1.8 kW Cu ceramic X-ray tube as X-ray source (Cu Kα irradiation) operating at 45 kV and 40 mA and PIXcel3D 2 × 2 as area detector, in the range 5°–80°, scan step size 0.013° and scan speed 0.094° s^{-1}.

Scanning electron microscopy (SEM) and scanning electron microscopy energy dispersive X-ray spectroscopy (SEM-EDX)

SEM images and elemental analysis by SEM-EDX were acquired using a Hitachi SU-70 system operating between 5 and 20 kV. The samples were prepared by drop casting the final product dispersed in hexane on a stainless-steel substrate stuck to the sample holder using a carbon tape. Image processing was done using the ImageJ software.[65]

X-ray photoelectron spectroscopy (XPS)

XPS spectra were measured using a Kratos AXIS ULTRA spectrometer fitted with a mono Al Kα (1486.58 eV) X-ray gun. C 1s line at 284.8 eV was used to perform calibration. Construction and peak fitting were performed using CasaXPS software.[66] Samples for XPS were prepared by drop-casting microrods dispersion in toluene on a p-type boron-doped silicon.

Reflectance measurements

Reflectance spectrum was measured by a Shimadzu UV–2600i spectrophotometer equipped with a $BaSO_4$ coated integrate sphere. The spectrum was acquired in the 200–1400 nm range, scan step size 1.0 nm, time for one scan 6 min (scan speed 0.0028 nm s^{-1}). The reflectance data were transformed using Kubelka–Munk function and Tauc plot was constructed to estimate the optical band gap.

Fourier transform infrared (FTIR) spectroscopy

FTIR spectra were acquired by FT-IR Nicolet iS20 spectrometer (Thermo Fisher Scientific) in attenuated total reflectance (ATR) mode, number of sample scans 32, collection length 95.44 s, resolution 4000 cm^{-1}, number of scan points 12 415, wavelength range 500–4000 cm^{-1}. The response was expressed as % transmittance. Powder and liquid samples were deposited directly onto the diamond crystal prior to spectral acquisition.

Conflicts of interest

There are no conflicts to declare.

Data availability

The data that support the findings of this study are available on request from the corresponding author. The data supporting this article (additional XRD and TEM data, XPS, FTIR, SAED) have been included as part of the supplementary information (SI). Supplementary information is available. See DOI: https://doi.org/10.1039/d5nr03842a.

Acknowledgements

F. L. and S. A. acknowledges the financial support by National Recovery and Resilience Plan (NRRP), Mission 4 Component 2 Investment 1.3—Call for tender No. 1561 of 11.10.2022 of Ministero dell'Università e della Ricerca (MUR); funded by the European Union– NextGenerationEU; Project code PE0000021, Concession Decree No. 1561 of 11.10.2022 adopted by the Ministero dell'Università e della Ricerca (MUR), CUP–D33C22001330002, Project title "Network 4 Energy Sustainable Transition–NEST". S. S. acknowledges Horizon TMA MSCA Postdoctoral Fellowship (Project ID 101207456). A. B. and M. P. acknowledge IRC (GOIPD/2024/600 and GOIPG/2024/3075) for funding. S. S and N. N. P. acknowledge the financial support of Taighde Éireann – Research Ireland under Grant number 22/FFP-P/11591.

References

1 U. V. Ghorpade, M. P. Suryawanshi, M. A. Green, T. Wu, X. Hao and K. M. Ryan, *Chem. Rev.*, 2022, **123**, 327–378.
2 S. Shyamal and N. Pradhan, *ACS Energy Lett.*, 2023, **8**, 3902–3926.
3 J. Olivier-Fourcade, J. C. Jumas, M. Maurin and E. Philippot, *Z. Anorg. Allg. Chem.*, 1980, **468**, 91–98.
4 V. I. Starosta, J. Kroutil and L. Beneš, *Cryst. Res. Technol.*, 1990, **25**, 1439–1442.
5 S. Sen, S. Bera, A. K. Guria and N. Pradhan, *J. Phys. Chem. C*, 2021, **125**, 1923–1928.
6 S. Sen, R. Jana, S. Bera, S. Shyamal, P. Sahu, A. Datta and N. Pradhan, *J. Phys. Chem. Lett.*, 2022, **13**, 3804–3811.
7 S. Bera, S. Shyamal, S. Sen and N. Pradhan, *J. Phys. Chem. C*, 2020, **124**, 15607–15615.
8 L. Protesescu, S. Yakunin, M. I. Bodnarchuk, F. Krieg, R. Caputo, C. H. Hendon, R. X. Yang, A. Walsh and M. V. Kovalenko, *Nano Lett.*, 2015, **15**, 3692–3696.
9 Q. A. Akkerman, G. Rainò, M. V. Kovalenko and L. Manna, *Nat. Mater.*, 2018, **17**, 394–405.
10 H. Zhang, Y. Xia, Y. Zhang, U. V. Ghorpade, M. He, S. W. Shin, X. Hao and M. P. Suryawanshi, *Adv. Sci.*, 2025, 2413131.
11 T. Li, X. Wang, Y. Yan and D. B. Mitzi, *J. Phys. Chem. Lett.*, 2018, **9**, 3829–3833.
12 A. Kojima, K. Teshima, Y. Shirai and T. Miyasaka, *J. Am. Chem. Soc.*, 2009, **131**, 6050–6051.
13 D. Amgar, T. Binyamin, V. Uvarov and L. Etgar, *Nanoscale*, 2018, **10**, 6060–6068.
14 A. Nyayban, S. Panda, A. Chowdhury and B. I. Sharma, *Mater. Today Commun.*, 2020, **24**, 101190.
15 S. Govinda, B. P. Kore, D. Swain, A. Hossain, C. De, T. N. Guru Row and D. D. Sarma, *J. Phys. Chem. C*, 2018, **122**, 13758–13766.
16 I. Levchuk, A. Osvet, X. Tang, M. Brandl, J. D. Perea, F. Hoegl, G. J. Matt, R. Hock, M. Batentschuk and C. J. Brabec, *Nano Lett.*, 2017, **17**, 2765–2770.
17 M. V. Kovalenko, L. Protesescu and M. I. Bodnarchuk, *Science*, 2017, **358**, 745–750.
18 L. Chouhan, S. Ghimire, C. Subrahmanyam, T. Miyasaka and V. Biju, *Chem. Soc. Rev.*, 2020, **49**, 2869–2885.
19 W.-J. Yin, T. Shi and Y. Yan, *J. Phys. Chem. C*, 2015, **119**, 5253–5264.
20 D. Madadi, *Mater. Chem. Phys.*, 2023, **308**, 128231.
21 M. T. Hörantner, T. Leijtens, M. E. Ziffer, G. E. Eperon, M. G. Christoforo, M. D. McGehee and H. J. Snaith, *ACS Energy Lett.*, 2017, **2**, 2506–2513.
22 L. Lei, Q. Dong, K. Gundogdu and F. So, *Adv. Funct. Mater.*, 2021, **31**, 2010144.
23 G. Xing, N. Mathews, S. S. Lim, N. Yantara, X. Liu, D. Sabba, M. Grätzel, S. Mhaisalkar and T. C. Sum, *Nat. Mater.*, 2014, **13**, 476–480.
24 B. Tang, H. Dong, L. Sun, W. Zheng, Q. Wang, F. Sun, X. Jiang, A. Pan and L. Zhang, *ACS Nano*, 2017, **11**, 10681–10688.
25 T. Yang, F. Li and R. Zheng, *ACS Appl. Electron Mater.*, 2019, **1**, 1348–1366.
26 Y. Wang, L. Song, Y. Chen and W. Huang, *ACS Photonics*, 2019, **7**, 10–28.

27 C. Peng, H. Yao, O. Ali, W. Chen, Y. Yang, Z. Huang, H. Liu, J. Li, T. Chen and Z. Li, *Nature*, 2025, 1–8.
28 M. Zeng, F. Locardi, D. Mara, Z. Hens, R. Van Deun and F. Artizzu, *Nanoscale*, 2021, **13**, 8118–8125.
29 D. N. Dirin and M. V. Kovalenko, *Chimia*, 2024, **78**, 862–868.
30 S. Toso, D. Baranov, C. Giannini and L. Manna, *ACS Nano*, 2021, **15**, 20341–20352.
31 B. Philippe, B.-W. Park, R. Lindblad, J. Oscarsson, S. Ahmadi, E. M. J. Johansson and H. Rensmo, *Chem. Mater.*, 2015, **27**, 1720–1731.
32 M. Ren, X. Qian, Y. Chen, T. Wang and Y. Zhao, *J. Hazard. Mater.*, 2022, **426**, 127848.
33 C. Y. Fong, C. Perlov and F. Wooten, *J. Phys. C: Solid State Phys.*, 1982, **15**, 2605.
34 A. N. Roth, A. P. Porter, S. Horger, K. Ochoa-Romero, G. Guirado, A. J. Rossini and J. Vela, *Chem. Mater.*, 2024, **36**, 4542–4552.
35 P. Henkel, J. Li, G. K. Grandhi, P. Vivo and P. Rinke, *Chem. Mater.*, 2023, **35**, 7761–7769.
36 A. Nicolson, J. Breternitz, S. R. Kavanagh, Y. Tomm, K. Morita, A. G. Squires, M. Tovar, A. Walsh, S. Schorr and D. O. Scanlon, *J. Am. Chem. Soc.*, 2023, **145**, 12509–12517.
37 R. Nie, K. S. Lee, M. Hu, M. J. Paik and S. Il Seok, *Matter*, 2020, **3**, 1701–1713.
38 S. R. Kavanagh, C. N. Savory, D. O. Scanlon and A. Walsh, *Mater. Horiz.*, 2021, **8**, 2709–2716.
39 J. He, X. Hu, Z. Liu, W. Chen and G. Longo, *Adv. Funct. Mater.*, 2023, **33**, 2306075.
40 H. J. Xiang, B. Huang, E. Kan, S.-H. Wei and X. G. Gong, *Phys. Rev. Lett.*, 2013, **110**, 118702.
41 Q. Wang, B. Xu, J. Sun, H. Liu, Z. Zhao, D. Yu, C. Fan and J. He, *J. Am. Chem. Soc.*, 2014, **136**, 9826–9829.
42 G. Volonakis, A. A. Haghighirad, R. L. Milot, W. H. Sio, M. R. Filip, B. Wenger, M. B. Johnston, L. M. Herz, H. J. Snaith and F. Giustino, *J. Phys. Chem. Lett.*, 2017, **8**, 772–778.
43 E. M. Hutter, M. C. Gélvez-Rueda, A. Osherov, V. Bulović, F. C. Grozema, S. D. Stranks and T. J. Savenije, *Nat. Mater.*, 2017, **16**, 115–120.
44 M. A. Green, A. Ho-Baillie and H. J. Snaith, *Nat. Photonics*, 2014, **8**, 506–514.
45 D. Quarta, D. M. Tobaldi and C. Giansante, *J. Phys. Chem. Lett.*, 2024, **15**, 7645–7651.
46 C. de Mello Donegá, P. Liljeroth and D. Vanmaekelbergh, *Small*, 2005, **1**, 1152–1162.
47 S. G. Kwon and T. Hyeon, *Small*, 2011, **7**, 2685–2702.
48 Cb. Murray, D. J. Norris and M. G. Bawendi, *J. Am. Chem. Soc.*, 1993, **115**, 8706–8715.
49 L. Manna, *Nano Lett.*, 2023, **23**, 9673–9676.
50 K. Vighnesh, S. Wang, H. Liu and A. L. Rogach, ACS Nano, 2022, **16**, 19618–19625.
51 D. Quarta, S. Toso, A. Fieramosca, L. Dominici, R. Caliandro, A. Moliterni, D. M. Tobaldi, G. Saleh, I. Gushchina and R. Brescia, *Chem. Mater.*, 2023, **35**, 9900–9906.
52 D. Quarta, S. Toso, G. Saleh, R. Caliandro, A. Moliterni, A. Griesi, G. Divitini, I. Infante, G. Gigli, C. Giannini, L. Manna and C. Giansante, *Chem. Mater.*, 2023, **35**, 1029–1036.
53 S. Toso, M. Imran, E. Mugnaioli, A. Moliterni, R. Caliandro, N. J. Schrenker, A. Pianetti, J. Zito, F. Zaccaria and Y. Wu, *Nat. Commun.*, 2022, **13**, 3976.
54 C. Yang, Z. Wang, G. He, H. Zhang and C. Liao, *ACS Appl. Nano Mater.*, 2022, **5**, 16033–16038.
55 A. N. Roth, J. Opare-Addo, E. Gi, S. Mena, G. Guirado, R. D. Schaller, E. A. Smith and J. Vela, *Chem. Mater.*, 2023, **35**, 2165–2172.
56 J.-M. Themlin, M. Chtaïb, L. Henrard, P. Lambin, J. Darville and J.-M. Gilles, *Phys. Rev. B: Condens. Matter Mater. Phys.*, 1992, **46**, 2460.
57 T.-Y. Tsai, P.-R. Yan and S.-H. Yang, *Nanoscale Res. Lett.*, 2016, **11**, 516.
58 G. Almeida, L. Goldoni, Q. Akkerman, Z. Dang, A. H. Khan, S. Marras, I. Moreels and L. Manna, *ACS Nano*, 2018, **12**, 1704–1711.
59 P. J. Corvan and J. J. Zuckerman, *Inorg. Chim. Acta*, 1979, **34**, L255–L258.
60 S. S. Chitnis, N. Burford, R. McDonald and M. J. Ferguson, *Inorg. Chem.*, 2014, **53**, 5359–5372.
61 C. J. Carmalt, D. Walsh, A. H. Cowley and N. C. Norman, *Organometallics*, 1997, **16**, 3597–3600.
62 H. Haldar, C. B. Yildiz and M. Majumdar, *ChemPlusChem*, 2023, **88**, e202300211.
63 D. Cucinotta, C. De Stefano, O. Giuffrè, G. Lando, D. Milea and S. Sammartano, *J. Mol. Liq.*, 2014, **200**, 329–339.
64 M. A. Boles, D. Ling, T. Hyeon and D. V. Talapin, *Nat. Mater.*, 2016, **15**, 141–153.
65 *'ImageJ'*, https://imagej.net/ij/.
66 *CasaXPS*, https://www.casaxps.com/.

